RESEARCH ARTICLE

NANO · MICRO small
www.small-journal.com

Controlling Surface Chemical Inhomogeneity of $Ni_2P/MoNiP_2/MoP$ Heterostructure Electrocatalysts for Efficient Hydrogen Evolution Reaction

Xiuming Bu, Di Yin, Dong Chen, Quan Quan, Zhe Yang, SenPo Yip, Chun-Yuen Wong, Xianying Wang,* and Johnny C. Ho**

Crystalline/amorphous phase engineering is demonstrated as a powerful strategy for electrochemical performance optimization. However, it is still a considerable challenge to prepare transition metal-based crystalline/amorphous heterostructures because of the low redox potential of transition metal ions. Herein, a facile H_2-assisted method is developed to prepare ternary $Ni_2P/MoNiP_2/MoP$ crystalline/amorphous heterostructure nanowires on the conductive substrate. The characterization results show that the content of the $MoNiP_2$ phase and the crystallinity of the MoP phase can be tuned by simply controlling the H_2 concentration. The obtained electrocatalyst exhibits a superior alkaline hydrogen evolution reaction performance, delivering overpotentials of 20 and 76 mV to reach current densities of 10 and 100 mA cm^{-2} with a Tafel slope of 30.6 mV dec^{-1}, respectively. The catalysts also reveal excellent stability under a constant 100 h operation, higher than most previously reported electrocatalysts. These striking performances are ascribed to the optimized hydrogen binding energy and favorable hydrogen adsorption/desorption kinetics. This work not only exhibits the potential application of ternary $Ni_2P/MoNiP_2/MoP$ crystalline/amorphous heterostructure nanowires catalysts for practical electrochemical water splitting, but also paves the way to prepare non-noble transition metal-based electrocatalysts with optimized crystalline/amorphous heterostructures.

1. Introduction

Electrochemical hydrogen evolution reaction (HER) provides one of the most attractive approaches to achieving clean and high-power density energy, drawing tremendous research interests in recent years.[1] Until now, due to the superior catalytic performance, noble metal-based electrocatalysts have served as state-of-the-art HER catalysts;[2–4] however, their scarcity and operational instability essentially limit the widespread practical application. In order to address these challenges, different transition metal-based oxides,[5,6] sulfides,[7,8] phosphides,[9,10] and selenides[11,12] have been developed and considered as alternative electrocatalysts for water electrolysis. One limitation is that their catalytic activity is still not sufficient, being less competitive than those of noble metal-based counterparts.

Among many latest advances, phase engineering of crystalline/amorphous heterostructure nanomaterials has revealed the effectiveness of manipulating different phase proportions in enhancing their electrochemical properties.[13,14] Specifically, since HER is a two-electron transfer process involving the adsorption and desorption of hydrogen intermediate (H_{ads}) on the catalyst surface, the catalytic performance significantly relies on the free energy of hydrogen adsorption (ΔG_H).[15] For crystalline/amorphous heterostructure nanomaterials, the chemically inhomogeneous composition and saturation bonds on

X. Bu, X. Wang
CAS Key Laboratory of Materials for Energy Conversion
Shanghai Institute of Ceramics
Chinese Academy of Sciences (SICCAS)
Shanghai 200050, P. R. China
E-mail: wangxianying@mail.sic.ac.cn

D. Yin, D. Chen, Q. Quan, J. C. Ho
Department of Materials Science and Engineering
City University of Hong Kong
Kowloon, Hong Kong SAR 999077, P. R. China
E-mail: johnnyho@cityu.edu.hk

Z. Yang, C.-Y. Wong
Department of Chemistry
City University of Hong Kong
Kowloon, Hong Kong SAR 999077, P. R. China
E-mail: acywong@cityu.edu.hk

S. Yip, J. C. Ho
Institute for Materials Chemistry and Engineering
Kyushu University
Fukuoka 816-8580, Japan

J. C. Ho
State Key Laboratory of Terahertz and Millimeter Waves
City University of Hong Kong
Kowloon, Hong Kong SAR 999077, P. R. China

The ORCID identification number(s) for the author(s) of this article can be found under https://doi.org/10.1002/smll.202304546

DOI: 10.1002/smll.202304546

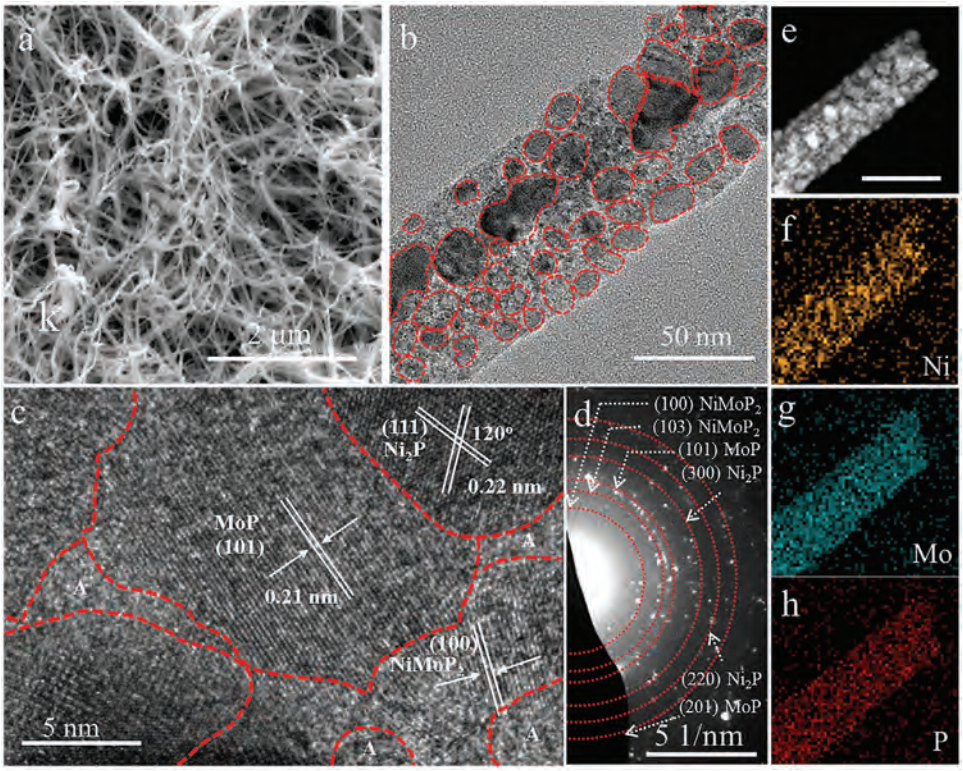

Figure 1. Physical characterization. a) SEM image, b) TEM image, c) HRTEM image, and corresponding d) SAED image of the NMP-10 sample. e) High-angle annular dark field (HAADF) STEM image and corresponding elemental mapping of f) Ni, g) Mo, and h) P of the NMP-10 catalyst, respectively. The scale bar in the (e) is 200 nm.

the surface may result in the ΔG_H variation over a wide range, affecting their electrochemical performance. For instance, Pd-based crystalline/amorphous heterostructure nanoplates were prepared with wet-chemical methods, where the characterization results showed their excellent ethanol oxidation reaction performance because of the coexistence of crystalline and amorphous structures, facilitating the formation of low-coordination atoms and causing changes in the electronic band structure of Pd atoms.[16] In addition, these wet-chemical methods can also be employed to construct ultrathin amorphous/crystalline Rh and bimetallic RhCu alloy nanosheets. These heterophase and alloying of Cu are beneficial for the electronic structure modulation of the active sites of Rh, thus resulting in the indole selectivity of over 99.9% with high activity.[17] Unfortunately, the synthesis of transition metal-based crystalline/amorphous heterostructures is less explored since the redox potential of transition metal ions is significantly lower than that of noble metal ions. Although there are few studies on the phase engineering of crystalline/amorphous heterostructure nanomaterials in the literature, an in-depth study about the effect of this specific phase engineering, namely, surface chemical inhomogeneity regulation, on the HER process is highly desirable but challenging.

In this work, we developed a facile H_2-assisted synthesis method to prepare crystalline/amorphous ternary $Ni_2P/MoNiP_2/MoP$ heterostructure nanowires on the conductive substrate. The physical characterization results show the content of $MoNiP_2$ phase and crystallinity of MoP phase can be tuned by simply controlling the H_2 concentration. The resultant electrocatalyst exhibits a significantly superior alkaline HER performance, delivering overpotentials of 20 and 76 mV to reach current densities of 10 and 100 mA cm^{-2} with a Tafel slope of 30.6 mV dec^{-1}, respectively. Also, the electrocatalyst displays excellent stability under a constant 100 h operation, which is higher than that of most previously reported counterparts. We experimentally demonstrated the superior performance can be attributed to the optimized hydrogen binding energy and favorable hydrogen adsorption/desorption kinetics. This work not only reveals the potential application of ternary $Ni_2P/MoNiP_2/MoP$ crystalline/amorphous heterostructure nanowires-based catalysts for larger-scale electrochemical water splitting, but also demonstrates the importance of phase engineering in the rational design and synthesis of heterostructure electrocatalysts.

2. Results and Discussion

The $Ni_2P/MoNiP_2/MoP$ ternary heterostructure was prepared by phosphating $NiMoO_4$ nanowires via NaH_2PO_2 at 500 °C in a mixed atmosphere of Ar/H_2 (190:10, v/v, denoted with NMP-10). The morphology of NMP-10 was first observed by scanning electron microscopy (SEM). It is found that the nickel foam substrate is completely covered with twisted nanowires with a diameter of ≈50 nm (**Figure 1**a). The transmission electron microscopy (TEM) image shows numerous protuberant crystalline nanoparticles (marked with red dotted circles) attached to the nanowire

backbone (Figure 1b). This observation indicates that the phosphorization process may trigger the segregation of Ni and Mo elements from the bimetallic oxide precursor, being consistent with the previous reports.[6,18] In addition, according to the high-resolution TEM (HRTEM) image as presented in Figure 1c, the lattice spacing of 0.22, 0.21, and 0.28 nm are ascribed to the (111) plane of Ni_2P (JCPDS No. 74–1385), (101) plane of MoP (JCPDS No. 65–6489), and (100) plane of $MoNiP_2$ (JCPDS No. 65–1985), respectively. At the same time, abundant crystalline/amorphous interfaces are observed on the surface of catalysts (amorphous area marked with A). The polycrystalline rings displayed in the selected area electron diffraction (SEAD) can be indexed to the (220) and (300) planes of Ni_2P, (100) and (103) planes of $MoNiP_2$, and (101) and (201) planes of MoP, accordingly (Figure 1d), further supporting the successful preparation of $Ni_2P/MoNiP_2/MoP$ ternary heterostructures. The elemental mapping reveals that within the NMP-10 nanowire, P and Mo elements are uniformly distributed while the Ni element is enriched in certain regions (Figure 1e–h), designating the obvious phase separation that occurred during the preparation process.

To further confirm the precise control of the crystalline/amorphous phase engineering, a series of samples were carefully fabricated by optimizing the H_2 concentration. Ni_2P/MoP was also prepared without introducing H_2 (denoted with NMP-0) for comparison. The morphology of NMP-0 was first observed by SEM (**Figure 2**a; Figures S1 and S2, Supporting Information). By contrast to the SEM image taken for the original $NiMoO_4$ nanowires (Figure S3, Supporting Information), almost no morphological changes were observed after phosphorylation. Also, nanowires, with a typical diameter of ≈150 nm, were aligned vertically and covered totally on the surface of the nickel foam substrate. As shown in the TEM image (Figure 2b), there are some crystalline nanoparticles (marked with red dotted circles) attached to the nanowire backbone, which is different from the smooth surface of $NiMoO_4$ (Figure S4, Supporting Information). The observed apparent phase separation phenomenon on the NMP-0 surface is due to the transformation of $NiMoO_4$ into the Ni-MoO_2 heterostructure (Ni nanoparticles anchored on the MoO_2 backbone) under high temperatures. At the same time, phosphorylation into Ni_2P/MoP occurs because of the existence of PH_3. The HRTEM image displays the intimate contact between Ni_2P and MoP. The lattice fringes of 0.30, 0.17, and 0.21 nm are well indexed to the (110) plane of Ni_2P, (110) and (101) planes of MoP, respectively (Figure 2c). In addition, SEAD can be indexed to the (111), (210), and (300) planes of Ni_2P and the (101) plane of MoP (Figure 2d). After introducing H_2 ($Ar:H_2$ = 195:5, v/v, denoted NMP-5), the nanowires became curved and decreased in diameter (≈87 nm, Figure 2e). Meanwhile, TEM images showed a significant increase in the density of giant highly crystalline nanoparticles on the amorphous backbone (Figure 2f). Surprisingly, a new phase of $NiMoP_2$ was observed in the HRTEM and SEAD results, where the lattice

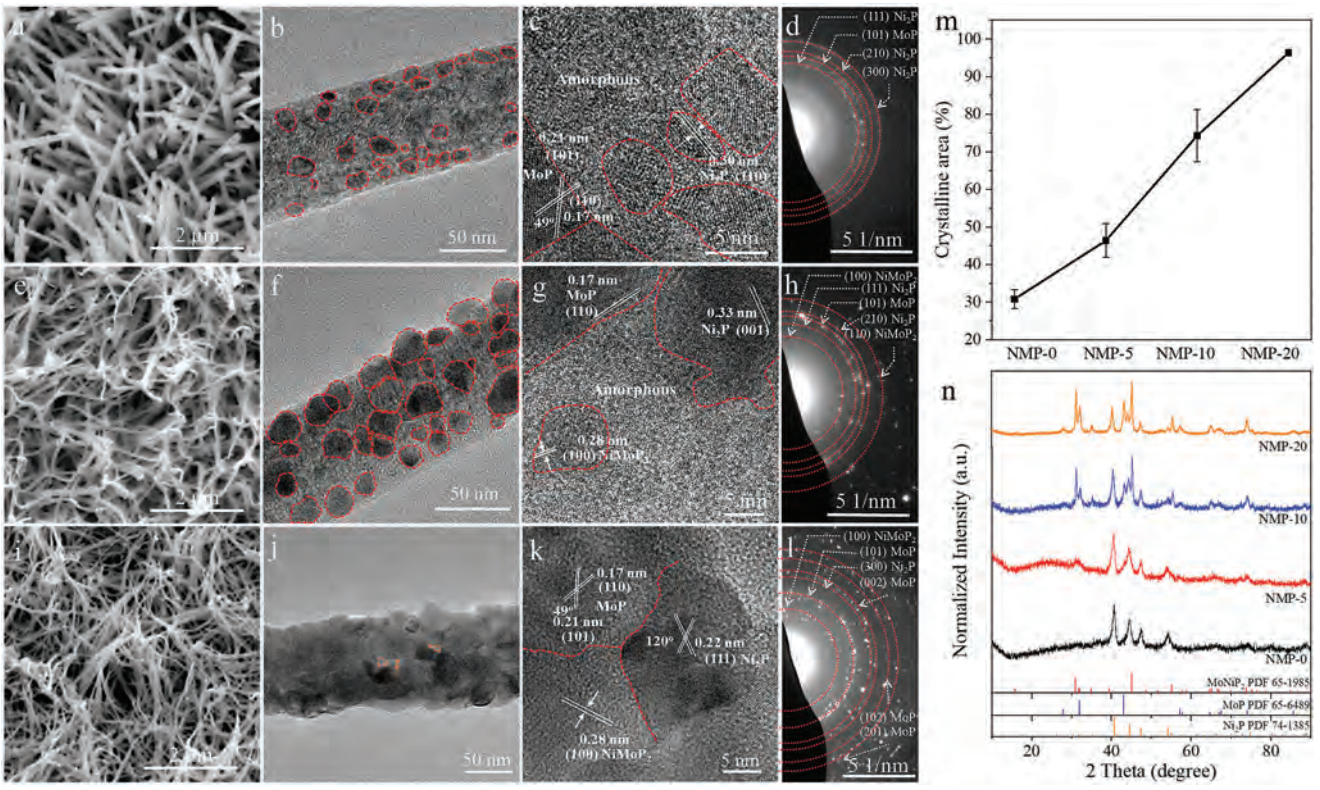

Figure 2. Structure evolution process. a) SEM image, b) TEM image, c) HRTEM image and corresponding, and d) SAED image of the NMP-0 sample. e) SEM image, f) TEM image, g) HRTEM image and corresponding h) SAED image of the NMP-5 sample. i) SEM image, g) TEM image, k) HRTEM image and corresponding l) SAED image of the NMP-20 sample. m) Summarized area ratio of the crystalline regions and n) XRD patterns of the prepared four samples.

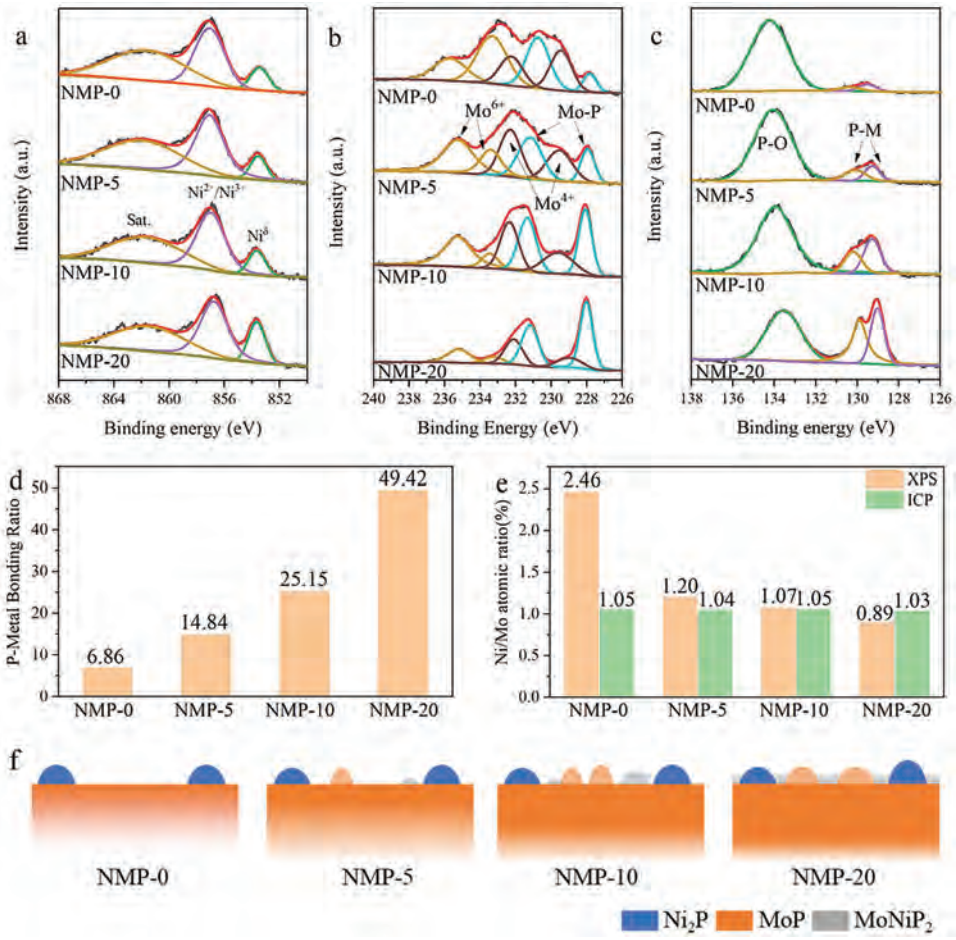

Figure 3. Surface electronic structure analysis. XPS spectra for a) Ni 2p, b) Mo 3d, and c) P 2p for these four samples, respectively. d) Calculated P–M bonding ratio and e) Ni/Mo ratio obtained from the XPS and ICP results. f) Schematics of the structure evolution diagram of the prepared electrocatalysts.

fringe space of 0.28 nm is assigned to the (100) plane of $NiMoP_2$ (Figure 2g,h). However, when the hydrogen flow rate increases to 20 sccm (denoted NMP-20), the nanowires aggregated, and the diameter slightly increased based on the statistics result (≈68 nm, Figure 2i). The TEM image shows that the nanowire backbone is almost entirely covered by a highly crystalline surface, with only small areas exhibiting amorphous features (Figure 2j, marked with orange dotted circles). The HRTEM image and SEAD result show that all Ni_2P, $MoNiP_2$, and MoP have high crystalline characteristics, and clear grain boundaries are observed (Figure 2k,l). Then a rough area ratio of the crystalline region was summarized in Figure 2m (Note S1, Supporting Information). It is clear that the crystalline/amorphous area ratio increases with the increase of hydrogen concentration in the gas mixture, which may be attributed to the fact that the hydrogen will be inserted into the Ni—P and Mo—P bonds, leading to the rearrangement of the Ni—P and Mo—P bonds that produce $NiMoP_2$ and improve the MoP crystallinity.[19] Moreover, this hydrogen concentration-dependent $NiMoP_2$ plays a decisive role in the crystallization/amorphous ratio. The above characterization results demonstrate that the H_2/PH_3 mixture significantly affects the surface chemical inhomogeneity. More phase and crystal structure information can be obtained in the X-ray diffraction (XRD) plots (Figure 2n; Note S2, Supporting Information). In the NMP-0 sample, compared with the crystalline peak of Ni_2P, the peak of MoP is weak, indicating that MoP is mainly present in the form of an amorphous phase, being consistent with the TEM result. After introducing hydrogen, a new phase of $MoNiP_2$ appears in the sample, and the crystallinity of MoP gets significantly increased, further indicating the successful phase engineering in the $Ni_2P/MoNiP_2/MoP$ ternary heterostructure.

Since phase engineering significantly affects the surface electronic structure of materials, X-ray photoelectron spectroscopy (XPS) is then performed to assess surface chemical compositions and chemical states of fabricated electrocatalysts. For Ni 2p spectra, the main peak located at 853.4, 857.0, and 861.8 eV can be ascribed to the Ni metallic peak, oxidized Ni^{2+}/Ni^{3+} peak, and satellite peak, respectively (**Figure 3**a).[20] With the increasing hydrogen flow rate, the apparent blue shift and increased Ni metallic peak intensity are observed in the spectra, indicating the electron transfer into the Ni atom in the coordination environment. In the Mo 3d spectra, the peak located at 235.7 eV as well as 233.4 eV are assigned to Mo^{6+}, the peaks at 232.3 and 229.5 eV are ascribed to Mo^{4+}, while the Mo–P peaks are centered at 230.8 and 227.8 eV, respectively (Figure 3b).[18] Meanwhile, with the increasing hydrogen concentration, the red shift phenomenon and increased

Mo–P peak in the Mo 3d spectra are witnessed, indicating the electron loss of Mo atoms. Regarding the P 2p spectra of the catalysts, the increase of the P–M peaks located at 129.3 and 130.3 eV indicates the controllable P–M bonding ratio in the electrocatalyst, posing a strong effect on the surface electronic structure (Figure 3c). Particularly, for the NMP-20 catalyst, the surface P–M bond ratio can reach 49.42% (Figure 3d; Table S1, Supporting Information). In addition, since the detection depth of the XPS technique is 3–10 nm, while the emission spectroscopy results of inductively coupled plasma (ICP) can give an overall composition analysis, combining these two characterization techniques can give more detailed information on the composition of the surface and the interior regions.[21] As shown in Figure 3e, the ICP results show that these catalysts' Ni/Mo ratio values remain almost constant. By contrast, the XPS results reveal that this value decreases continuously with the increasing hydrogen ratio, indicating the outward migration of Mo atoms due to the reaction between MoP and Ni_2P. Combined with the previous analysis, the electrocatalyst's surface structure and composition evolution is proposed, as shown in Figure 3f. When only PH_3 is introduced, Ni atoms' outward migration and phosphorylation occur simultaneously, and highly crystalline Ni_2P nanoparticles are formed on the surface. While for the Mo atoms, only a small fraction of Mo atoms is precipitated from the backbone to form the crystalline MoP phase (XRD result for NMP), and most of the Mo atoms react with PH_3 to form an amorphous MoP nanowire backbone. Once hydrogen is introduced into the system, the Mo atoms become active, resulting in the crystalline improvement of MoP. More importantly, the reaction barrier between MoP and Ni_2P is decreased, and a new phase $MoNiP_2$ is formed on the interface of the MoP/Ni_2P heterostructure. With the increasing hydrogen concentration, the increased crystallinity of all phases and enhanced relative $MoNiP_2$ content are confirmed until the surface of the catalyst is completely covered with the highly crystalline phase.

To shed light on the superior electrochemical characteristics induced by phase engineering, the electrocatalytic HER performance of the prepared materials is measured in the 1.0 M KOH electrolyte. **Figure 4**a shows the polarization curves of the samples. NMP-10 exhibits a remarkable HER performance, whose current density increases rapidly along the increasing potential. The overpotential for NMP-10 to achieve 10 mA cm^{-2} catalytic current density is 20 mV, which is much lower than that of NMP-5 (53 mV), NMP-20 (67 mV), and NMP-0 (85 mV). More importantly, as depicted in Figure 4b, only 76 mV is needed for NMP-10 to reach 100 mA cm^{-2}, indicating excellent electrocatalytic performance. From the point of view of HER kinetics evaluated by Tafel plots, the NMP-10 catalyst delivers the lowest slope value of 30.6 mV dec^{-1}, outperforming the NMP-5 catalyst (56.8 mV dec^{-1}), NMP-20 catalyst (76.1 mV dec^{-1}), and NMP-0 catalyst (119.8 mV dec^{-1}), implying the superior reaction kinetics for the NMP-10 catalyst (Figure 4c). Moreover, the Tafel slope of NMP-10 is close to 30 mV dec^{-1}, denoting the HER kinetic process mainly governed by the water dissociation step ($M + H_2O + e \rightarrow MH_{ads} + OH^-$, M stands for catalyst, i.e., Volmer–Tafel mechanism).[22] By contrast, the Tafel slopes of NMP-5, NMP-20, and NMP-0 fall into the range of 40–120 mV dec^{-1}, indicating the rate-determining step being insufficient hydrogen intermediate combination ($MH_{ads} + H_2O + e\text{-} \rightarrow M + H_2 + OH^-$, i.e., Volmer–Heyrovsky step).[22,23] It is also worth noting that the improved HER performance is not observed with the increasing $MoNiP_2$ content. This way, the improvement in the HER performance must be due to the synergistic effect among multiple components with the detailed synergistic effect discussed later. In addition, electrochemical impedance spectroscopy (EIS), as shown in Figure 4d, is further employed to investigate the HER kinetics at the interface between electrodes and electrolytes of the samples. The recorded Nyquist plots are simulated by a double-parallel equivalent circuit model, where R_{ct} reflects the charge-transfer kinetics (insets of Figure 4d), and the values of 10.36, 66.18, 76.89, and 133.70 Ω for the NMP-10, NMP-5, NMP-20, and NMP-0 samples suggest that a lower charge transfer resistance is the reason for the improved HER performance.[24] Moreover, to evaluate the electrochemical surface area of the fabricated catalysts, electrochemical double-layer capacitances (C_{dl}) of the catalysts are measured via a simple cyclic voltammetry (CV) method (Figure S5, Supporting Information), where C_{dl} is considered to be directly proportional to the catalysts' effective surface area. It can be seen from Figure 4e that the C_{dl} values are measured to be ≈12.9, 8.4, 7.1, and 3.4 mF cm^{-2} for the NMP-10, NMP-5, NMP-20, and NMP-0 samples, respectively, suggesting that the NMP-10 catalyst has a more active surface area. When the specific current density is normalized with respect to ECSA, NMP-10 exhibits a much higher specific current density than those of other catalysts for the entire voltage range measured (Figure 4f), further confirming that the NMP-10 catalyst is indeed intrinsically more active than the NMP-5, NMP-20, and NMP-0 catalysts.[25] Remarkably, our electrocatalyst exhibited excellent electrochemical performance in terms of overpotential and Tafel slopes compared with most recently reported catalysts, even for some noble metal-based catalysts (Figure 4g).[6,26–38] The durability of the catalyst is then investigated under electrocatalytic operation. Particularly, we measure the practical operation of the NMP-10 catalyst via electrolysis at a fixed cathodic current density (≈100 and 500 mA cm^{-2}). No obvious degradation has been observed for electrolysis even after a long period of 100 h, suggesting the potential of using these catalysts over a long duration in an electrochemical process. In addition, the SEM, TEM, HRTEM, and XPS results of NMP-10 after 100 h of HER were characterized, exhibiting a typical metal phosphide characteristic (Figure S6, Supporting Information).[39,40] It should be noticed that the amorphous area in the sample increased obviously due to the in situ surface reconstruction process.

According to systematic experimental work and density functional theory (DFT) theoretical calculations, hydrogen binding energy (HBE) can be used as a descriptor of HER performance. Therefore, in order to explore the activity mechanism of the obtained catalysts in depth, correlation studies between HER activity and experimentally measured HBE were constructed using ultraviolet photoelectron spectroscopy (UPS) spectroscopy and CV methods. First, the valence-state structure of the prepared catalysts is examined using UPS. The electron bands of all samples crossed the Fermi level (**Figure 5**a), suggesting their metallic nature. The peaks next to the Fermi level correspond to the metallic Ni 3d states.[41] The positions of their binding energy are far from the Fermi level in the following order: NMP-0 < NMP-20 < NMP-5 < NMP-10. Based on the d-band theory, a downshifted d-band would result in a weakened adsorption strength.[42]

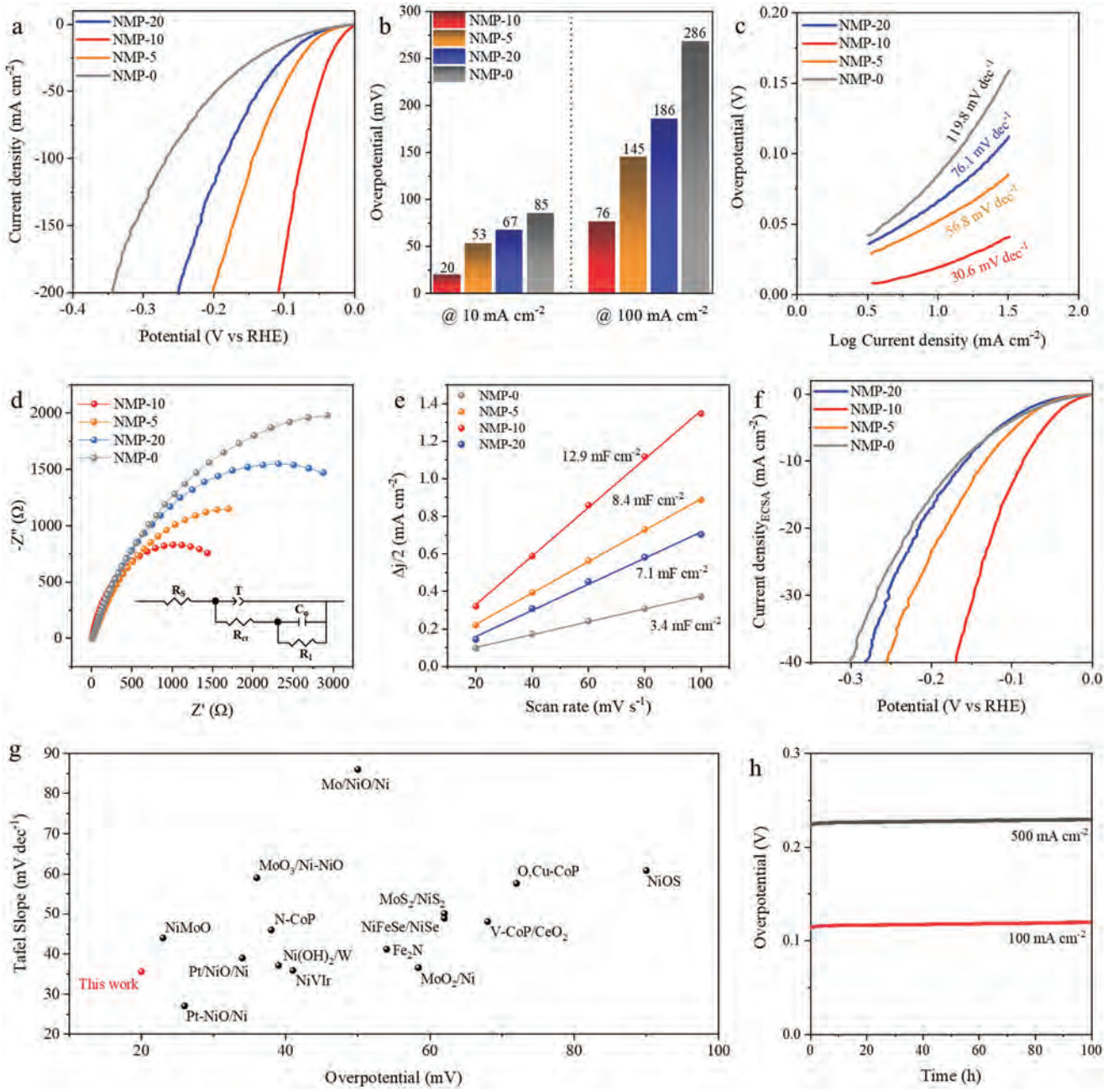

Figure 4. Electrochemical performance of as-made electrocatalysts for HER in 1 M KOH. a) Polarization curves with *iR* compensation. b) Overpotential values when the current density is 10 and 100 mA cm^{-2}, respectively. c) Their corresponding Tafel plots, d) EIS spectra, e) difference in the current density plotted against the scan rate at −0.55 V versus Ag/AgCl, and f) ECSA normalized current densities of the prepared samples. g) Comparison of overpotentials and Tafel slopes at 10 mA cm^{-2} for the NMP-10 catalyst with recent reported active HER electrocatalysts. h) Stability test of the NMP-10 catalyst.

Therefore, the order of HBE is: NMP-0 > NMP-20 > NMP-5 > NMP-10. Furthermore, the HBE of active sites can be directly correlated with the potential of under-potentially deposited hydrogen desorption peak (E_{peak}) via $\Delta H = -FE_{peak}$, which yields a low HBE of −0.23 eV for NMP-10 as compared with that of NMP-5 (−0.29 eV), NMP-20 (−0.30 eV), and NMP (−0.34 eV) (Figure 5b), which is consistent with the UPS results.[43] In this case, a weaker H chemisorption strength of NMP-10 compared to other catalysts induces the acceleration of the hydrogen desorption behavior. Then, the hydrogen adsorption behavior on the catalysts is also investigated via the operando EIS technique since the second parallel components (C_φ and R_1) can reveal the hydrogen adsorption behavior on the catalyst surface, where R_1 and C_φ reflect the hydrogen adsorption resistance and pseudocapacitance, respectively (inset of Figure 4d; Figure S7, Table S2, Supporting Information).[44] As shown in Figure 5c, the C_φ versus η curves

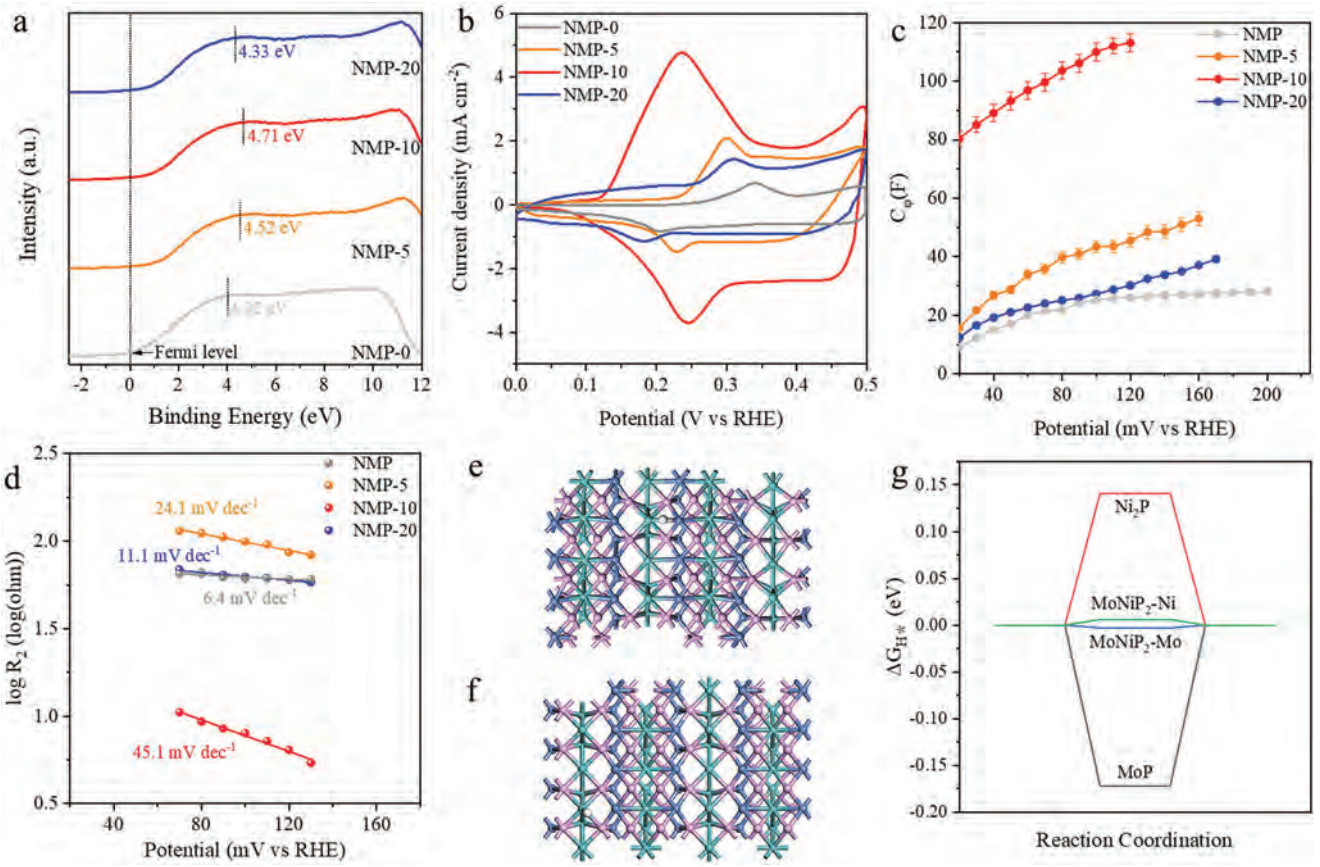

Figure 5. Mechanism analysis. a) UPS spectra and b) CV curves recorded at 0–0.5 V (vs RHE) of the prepared catalysts. c) Plots of C_{φ} versus η of the catalysts during HER in 1 M KOH. d) EIS-derived Tafel plots of the catalysts obtained from the hydrogen adsorption resistance, R_2. Hydrogen adsorbed at e) Ni and f) Mo sites, respectively. g) The calculated hydrogen adsorption free energy changes for Ni_2P, MoP, $MoNiP_2$-Ni, and $MoNiP_2$-Mo. White: H; Blue: Ni; Green: Mo; Pink: P.

provide the hydrogen adsorption charge information on the catalyst surface during HER process. The highest C_{φ} value of NMP-10 indicates the highest H_{ads} coverage on the surface among the prepared samples, which is consistent with the Tafel slope analysis. In this way, the corresponding hydrogen adsorption kinetics on the electrode surface has also changed. Given the potential dependent R_1 of all catalysts, it is reasonable to quantify their hydrogen adsorption kinetics by plotting log R_1 versus η and calculating the EIS-derived Tafel slopes under Ohm's law.[41] As shown in Figure 5d, the obviously decreased EIS-derived Tafel slope for NMP-10 demonstrates enhanced hydrogen adsorption kinetics. Overall, the detailed experiment results demonstrate the controllable surface chemical inhomogeneity in the ternary heterostructure, optimizing the HER process via accelerating the hydrogen intermediate adsorption and desorption kinetics.

To gain more insights, theoretical calculations were employed to explore the role of each component in the HER process (Figure S8). Hydrogen intermediates were located at the possible active site, and the corresponding free energy diagram was obtained accordingly. The Gibbs free energies of MoP and Ni_2P are −0.172 and 0.141 eV, respectively, which is consistent with the data reported by Jaramilloit's work.[45] For $MoNiP_2$, the Ni and Mo sites are both the potential active sites for HER (Figure 5e,f). DFT calculations show the free energies of H adsorption for Ni and Mo sites on the $MoNiP_2$ surface are 0.006 and −0.003 eV, respectively, close to 0, which proves that the intrinsic catalytic activity of $MoNiP_2$ is much higher than that of Ni_2P and MoP (Figure 5g). According to the Sabatier principle, Gibbs free energy's negative and positive values indicate that H intermediates are adsorption-prone and detachment-prone on the catalyst surface, respectively.[46] Therefore, in this work, we consider that $MoNiP_2$ is the main catalyst for the HER process and that MoP and Ni_2P synergistically work together to enhance the catalytic performance. Consequently, in the beginning, with the increase of the hydrogen/argon ratio, the increased proportion of $MoNiP_2$ significantly improves the catalytic activity. While for the sample NMP-20, the surface of the catalyst is almost all crystalline regions, and according to previous studies, the performance of crystalline catalysts is much lower than that of amorphous catalysts.[47] Therefore, in this work, both the component content and the amorphous/crystalline exposed area ratio play an extremely important role in dictating the catalyst's performance.

3. Conclusion

In this work, we developed a facile H_2-assisted method to prepare ternary $Ni_2P/MoNiP_2$/MoP crystalline/amorphous heterostructure nanowires on the conductive substrate. Based on various

characterization techniques, the content of the $MoNiP_2$ phase and the crystallinity of the MoP phase can be tuned by simply controlling the H_2 concentration. The optimized surface chemical inhomogeneity yields a proper hydrogen binding energy and favorable hydrogen adsorption/desorption kinetics. Thus, the obtained electrocatalyst exhibits a superior alkaline HER performance, delivering overpotentials of 20 and 76 mV to reach current densities of 10 and 100 mA cm^{-2} with a Tafel slope of 30.6 mV dec^{-1}, respectively. Importantly, the catalysts give excellent stability under a constant 100 h operation, higher than most previously reported electrocatalysts. This work not only exhibits the potential application of ternary $Ni_2P/MoNiP_2/MoP$ crystalline/amorphous heterostructure nanowires catalysts for practical larger-scale electrochemical water splitting, but also demonstrates the importance of phase engineering in the rational design and synthesis of heterostructure electrocatalysts.

4. Experimental Section

Preparation of $Ni_2P/MoNiP_2/MoP$ Ternary Heterostructure Nanowires on Nickel Foams: In this work, all nickel foams were treated as follows: acetone treatment, hydrochloric acid (2 M), deionized water treatment, and ethanol treatment for 10 min, respectively. Typically, 0.5 mmol $NiCl_2$ and 0.5 mmol Na_2MoO_4 were added to 15 mL of deionized water and mixed well. Then, a piece of nickel foam and the homogenous solution were sealed into a Teflon-lined stainless steel autoclave heated at 160 °C for 6 h in an electric oven. After the hydrothermal treatment, the resulting nickel foam covered with $NiMoO_4$ nanowires was washed with deionized water and ethanol under ultrasonication several times, followed by drying in a vacuum oven at 80 °C overnight.

Then, $NiMoO_4$ nanowires/nickel foam and 800 mg of NaH_2PO_2 were put into two separate positions of the quartz boat, with the NaH_2PO_2 powder located on the upstream side of the gas. Then, the samples were treated at 500 °C for 2 h with a heating rate of 2.5 °C min^{-1} under Ar/H_2 atmosphere, and the flow rate was adjusted to 200/0 (NMP), 195/5 (NMP-5), 190/10 (NMP-10), and 180/20 (NMP-20) sccm, respectively. The final product was obtained after cooling to room temperature.

The mass loading of the NMP-10, NMP-5, NMP-20, and NMP-0 was carefully confirmed by a microbalance, which is 15.2, 17.4, 18.2, and 18.4 mg cm^{-2}, respectively.

Material Characterization: The prepared samples were characterized by SEM (Phenom-World, The Netherlands), field-emission SEM (SU-8010, Hitachi, Tokyo, Japan), Bruker D2 Phaser (Bruker, Billerica, MA, USA) instrument equipped with a monochromatized Cu–Kα radiation, TEM, and HRTEM (Tecnai G2 F30, FEI, Hillsboro, OR, USA), and XPS (VG Multilab 2000, Thermo Fisher Scientific, Waltham, MA, USA). SPECS Leybold EA 11 MCD hemispherical electron analyzer was employed to acquire UPS He II spectra with an excitation energy of 40.82 eV. The binding energy scale was referenced to the Fermi level of the Au sample. The area and perimeter of the crystalline particle were counted with the software ImageJ.

Electrochemical Measurement: All electrochemical characterization was surveyed via Gamry 300 electrochemical workstation with a conventional three-electrode cell at room temperature. The prepared sample, saturated calomel electrode, and a carbon rod were employed as the working electrode, the reference electrode, and the counter electrode, respectively. The active area of the electrocatalyst immersed in the electrolyte was defined by applying a silicon rubber. All potentials calibrated are versus the reversible hydrogen electrode (RHE). The activities of HER were investigated in 1 M KOH aqueous solution (pH = 14) with a scan rate of 5 mV s^{-1}. EIS investigations were conducted in the 100 kHz to 0.1 Hz frequency range at various HER potentials.

DFT Calculations: Vienna ab initio Simulation Package and the Perdew–Burke–Ernzerhof functional within generalized gradient approximation were carried out to perform DFT calculations. The projector augment wave method was applied in plane waves with a cutoff energy of 500 eV. All geometry optimizations were converged with a Hellmann–Feynman force smaller than 0.02 eV $Å^{-1}$ and a total energy change smaller than 10^{-5} eV. KPoints were automatically generated via vaspkit.

Supporting Information

Supporting Information is available from the Wiley Online Library or from the author.

Acknowledgements

This work was sponsored by Shanghai Sailing Program (Project Nos. 23YF1455000) and the City University of Hong Kong (Project Nos. 9667227 and 7005944).

Conflict of Interest

The authors declare no conflict of interest.

Author Contributions

X.M.B., X.Y.W., and J.C.H. proposed the concept and cowrote the manuscript. X.M.B. performed the experiment. All authors participated in data analysis and manuscript discussion.

Data Availability Statement

The data that support the findings of this study are available from the corresponding author upon reasonable request.

Keywords

electrocatalysts, heterostructures, hydrogen evolution reaction, surface chemical inhomogeneity

Received: May 30, 2023
Revised: July 25, 2023
Published online: August 25, 2023

[1] X. Zou, Y. Zhang, *Chem. Soc. Rev.* **2015**, *44*, 5148.
[2] J. N. Hansen, H. Prats, K. K. Toudahl, N. Mørch Secher, K. Chan, J. Kibsgaard, I. Chorkendorff, *ACS Energy Lett.* **2021**, *6*, 1175.
[3] S. Ye, F. Luo, Q. Zhang, P. Zhang, T. Xu, Q. Wang, D. He, L. Guo, Y. Zhang, C. He, X. Ouyang, M. Gu, J. Liu, X. Sun, *Energy Environ. Sci.* **2019**, *12*, 1000.
[4] Z. Li, Y. Feng, Y. L. Liang, C. Q. Cheng, C. K. Dong, H. Liu, X. W. Du, *Adv. Mater.* **2020**, *32*, 1908521.
[5] M. Yang, Y. Jiang, M. Qu, Y. Qin, Y. Wang, W. Shen, R. He, W. Su, M. Li, *Appl Catal B* **2020**, *269*, 118803.
[6] X. Liu, K. Ni, C. Niu, R. Guo, W. Xi, Z. Wang, J. Meng, J. Li, Y. Zhu, P. Wu, Q. Li, J. Luo, X. Wu, L. Mai, *ACS Catal.* **2019**, *9*, 2275.
[7] A. Muthurasu, V. Maruthapandian, H. Y. Kim, *Appl. Catal. B* **2019**, *248*, 202.
[8] M. Wang, W. Zhang, F. Zhang, Z. Zhang, B. Tang, J. Li, X. Wang, *ACS Catal.* **2019**, *9*, 1489.

[9] X. Bu, R. Wei, W. Gao, C. Lan, J. C. Ho, *J. Mater. Chem. A* **2019**, *7*, 12325.
[10] A. Parra-Puerto, K. L. Ng, K. Fahy, A. E. Goode, M. P. Ryan, A. Kucernak, *ACS Catal.* **2019**, *9*, 11515.
[11] H. Zhou, F. Yu, Y. Liu, J. Sun, Z. Zhu, R. He, J. Bao, W. A. Goddard, S. Chen, Z. Ren, *Energy Environ. Sci.* **2017**, *10*, 1487.
[12] X. Xu, H. Liang, F. Ming, Z. Qi, Y. Xie, Z. Wang, *ACS Catal.* **2017**, *7*, 6394.
[13] Y. Chen, Z. Lai, X. Zhang, Z. Fan, Q. He, C. Tan, H. Zhang, *Nat. Rev. Chem.* **2020**, *4*, 243.
[14] H. Li, X. Zhou, W. Zhai, S. Lu, J. Liang, Z. He, H. Long, T. Xiong, H. Sun, Q. He, Z. Fan, H. Zhang, *Adv. Energy Mater.* **2020**, *10*, 2002019.
[15] Z. W. She, J. Kibsgaard, C. F. Dickens, I. Chorkendorff, J. K. Nørskov, T. F. Jaramillo, *Science* **2017**, *80*, 355.
[16] P. F. Yin, M. Zhou, J. Chen, C. Tan, G. Liu, Q. Ma, Q. Yun, X. Zhang, H. Cheng, Q. Lu, B. Chen, Y. Chen, Z. Zhang, J. Huang, D. Hu, J. Wang, Q. Liu, Z. Luo, Z. Liu, Y. Ge, X. J. Wu, X. W. Du, H. Zhang, *Adv. Mater.* **2020**, *32*, 2000482.
[17] J. Ge, P. Yin, Y. Chen, H. Cheng, J. Liu, B. Chen, C. Tan, P. F. Yin, H. X. Zheng, Q. Q. Li, S. Chen, W. Xu, X. Wang, G. Wu, R. Sun, X. H. Shan, X. Hong, H. Zhang, *Adv. Mater.* **2021**, *33*, 2006711.
[18] J. Zhao, B. Fu, X. Li, Z. Ge, B. Ma, Y. Chen, *ACS Appl. Energy Mater.* **2020**, *3*, 10910.
[19] S. Sriraman, S. Agarwal, E. S. Aydil, *Nature* **2002**, *418*, 62.
[20] P. F. Liu, X. Li, S. Yang, M. Y. Zu, P. Liu, B. Zhang, L. R. Zheng, H. Zhao, H. G. Yang, *ACS Energy Lett.* **2017**, *2*, 2257.
[21] X. Bu, R. Wei, Z. Cai, Q. Quan, H. Zhang, W. Wang, F. Li, S. Po, Y. Meng, K. Sum, X. Wang, *Appl. Surf. Sci.* **2021**, *538*, 147977.
[22] J. Zhang, W. Xiao, P. Xi, S. Xi, Y. Du, D. Gao, J. Ding, *ACS Energy Lett.* **2017**, *2*, 1022.
[23] X. Bu, X. Liang, Y. Bu, Q. Quan, Y. Meng, Z. Lai, W. Wang, C. Liu, J. Lu, C. M. Lawrence Wu, J. C. Ho, *Chem. Eng. J.* **2022**, *438*, 135379.
[24] J. Li, H. X. Liu, W. Gou, M. Zhang, Z. Xia, S. Zhang, C. R. Chang, Y. Ma, Y. Qu, *Energy Environ. Sci.* **2019**, *12*, 2298.
[25] S. Sun, H. Li, Z. J. Xu, *Joule* **2018**, *2*, 1024.
[26] Z. J. Chen, G. X. Cao, L. Y. Gan, H. Dai, N. Xu, M. J. Zang, H. Bin Dai, H. Wu, P. Wang, *ACS Catal.* **2018**, *8*, 8866.
[27] K. Xu, Y. Sun, Y. Sun, Y. Zhang, G. Jia, Q. Zhang, L. Gu, S. Li, Y. Li, H. J. Fan, *ACS Energy Lett.* **2018**, *3*, 2750.
[28] S. Li, C. Xi, Y. Z. Jin, D. Wu, J. Q. Wang, T. Liu, H. Bin Wang, C. K. Dong, H. Liu, S. A. Kulinich, X. W. Du, *ACS Energy Lett.* **2019**, *4*, 1823.
[29] L. Yang, R. Liu, L. Jiao, *Adv. Funct. Mater.* **2020**, *30*, 1909618.
[30] Y. Wu, J. Cai, Y. Xie, S. Niu, Y. Zang, S. Wu, Y. Liu, Z. Lu, Y. Fang, Y. Guan, X. Zheng, J. Zhu, X. Liu, G. Wang, Y. Qian, *Adv. Mater.* **2020**, *32*, 1904354.
[31] X. Li, Y. Wang, J. Wang, Y. Da, J. Zhang, L. Li, C. Zhong, Y. Deng, X. Han, W. Hu, *Adv. Mater.* **2020**, *32*, 2003414.
[32] J. Lin, P. Wang, H. Wang, C. Li, X. Si, J. Qi, J. Cao, Z. Zhong, W. Fei, J. Feng, *Adv. Sci.* **2019**, *6*, 1900246.
[33] G. Yilmaz, C. F. Tan, Y. F. Lim, G. W. Ho, *Adv. Energy Mater.* **2019**, *9*, 1802983.
[34] J. Li, D. Chu, D. R. Baker, R. Jiang, *J. Mater. Chem. A* **2022**, *10*, 1278.
[35] Y. Tang, L. Dong, H. Bin Wu, X. Y. Yu, *J. Mater. Chem. A* **2021**, *9*, 1456.
[36] J. Huang, J. Han, T. Wu, K. Feng, T. Yao, X. Wang, S. Liu, J. Zhong, Z. Zhang, Y. Zhang, B. Song, *ACS Energy Lett.* **2019**, *4*, 3002.
[37] Z. Wang, J. Chen, E. Song, N. Wang, J. Dong, X. Zhang, P. M. Ajayan, W. Yao, C. Wang, J. Liu, J. Shen, M. Ye, *Nat. Commun.* **2021**, *12*, 5960.
[38] K. L. Zhou, Z. Wang, C. B. Han, X. Ke, C. Wang, Y. Jin, Q. Zhang, J. Liu, H. Wang, H. Yan, *Nat. Commun.* **2021**, *12*, 5960.
[39] X. Xu, X. Tian, Z. Zhong, L. Kang, J. Yao, *J. Power Sources* **2019**, *424*, 42.
[40] X. Zou, Y. Wu, Y. Liu, D. Liu, W. Li, L. Gu, H. Liu, P. Wang, L. Sun, Y. Zhang, *Chem* **2018**, *4*, 1139.
[41] W. Ni, T. Wang, F. Héroguel, A. Krammer, S. Lee, L. Yao, A. Schüler, J. S. Luterbacher, Y. Yan, X. Hu, *Nat. Mater.* **2022**, *21*, 804.
[42] Z. J. Zhao, S. Liu, S. Zha, D. Cheng, F. Studt, G. Henkelman, J. Gong, *Nat. Rev. Mater.* **2019**, *4*, 792.
[43] Q. Wang, C. Q. Xu, W. Liu, S. F. Hung, H. B. Yang, J. Gao, W. Cai, H. M. Chen, J. Li, B. Liu, *Nat. Commun.* **2020**, *11*, 4246.
[44] J. Li, J. Hu, M. Zhang, W. Gou, S. Zhang, Z. Chen, Y. Qu, Y. Ma, *Nat. Commun.* **2021**, *12*, 3502.
[45] J. Kibsgaard, C. Tsai, K. Chan, J. D. Benck, J. K. Nørskov, F. Abild-Pedersen, T. F. Jaramillo, *Energy Environ. Sci.* **2015**, *8*, 3022.
[46] N. Danilovic, R. Subbaraman, D. Strmcnik, V. R. Stamenkovic, N. M. Markovic, *J. Serb. Chem. Soc.* **2013**, *78*, 2007.
[47] A. Indra, P. W. Menezes, N. R. Sahraie, A. Bergmann, C. Das, M. Tallarida, D. SchmeiBer, P. Strasser, M. Driess, *J. Am. Chem. Soc.* **2014**, *136*, 17530.